Structural, mechanical, and electronic properties of TaB$_2$, TaB, IrB$_2$, and IrB: First-principle calculations

Wen Jie Zhao, Yuan Xu Wang *

Institute for Computational Materials Science, School of Physics and Electronics, Henan University, Kaifeng 475004, People's Republic of China

ARTICLE INFO

ABSTRACT

First-principle calculations were performed to investigate the structural, elastic, and electronic properties of TaB$_2$, TaB, IrB$_2$, and IrB. The calculated equilibrium structural parameters, shear modulus, and Young's modulus of TaB$_2$ are well consistent with the available experimental data, and TaB$_2$ with $P6/mmm$ space group has stronger directional bonding between ions than WB$_2$, OsB$_2$, IrN$_2$, and PtN$_2$. For TaB$_2$, the hexagonal $P6/mmm$ structure is more stable than the orthorhombic $Pmmn$ one, while for IrB$_2$ the orthorhombic $Pmmn$ structure is the most stable one. The high shear modulus of $P6/mmm$ phase TaB$_2$ is mainly due to the strong covalent π-bonding of B-hexagon in the (0001) plane. Such a B-hexagon network can strongly resist against an applied [11$\bar{2}$0] (0001) shear deformation. Correlation between the hardness and the elastic constants of TaB$_2$ was discussed. The band structure shows that $P6/mmm$ phase TaB$_2$ and $Pmmn$ phase IrB$_2$ are both metallic. The calculations show that both TaB and IrB are elastically stable with the hexagonal $P6_3/mmc$ structure.

1. Introduction

Transition metal borides are of great interest in both fundamental science and technical application [1–14]. Experimentally, ReB$_2$ and WB$_2$ are found in the hexagonal phase with $P6_3/mmc$ and $P6/mmm$ space group [12–14]. Theoretically, Hao et al. confirmed that ReB$_2$ and WB$_2$ can be regarded as potential candidates of ultra-incompressible and hard materials [1]. Recently, osmium diboride has been synthesized by Cumberland et al. [2]. Their results indicated that OsB$_2$ is an ultra-incompressible material. The calculations by Wang show that hexagonal TcB$_2$ is a potential superhard material in term of its large elastic modulus and large G/B value [7]. Gu et al. [11] synthesized WB$_4$ and the measured average hardness is very high exceeding 46.2 GPa, comparable to that (45–50 GPa) of c-BN. Wang et al. predicted that five other transition metal B compounds (TMB$_4$, TM = Re, Mo, Ta, Os, and Tc) with the WB$_4$ structure are potential superhard materials [9].

TaB$_2$, similar to ZrB$_2$ and HfB$_2$, has the hexagonal AlB$_2$-like structure ($P6/mmm$) [15]. The experimental lattice constants are $a = 3.088$ A, $c = 3.241$ A in Ref. [16] and $a = 3.082$ A, $c = 3.243$ A in Ref. [17]. TaB$_2$ has a high melting point (3200 °C) [18], high

hardness (24.5 GPa) [19], good thermal and electrical conductivity, and resistance to most acids and bases [18]. Recently, phase pure TaB$_2$ powder was synthesized using reduction of Ta$_2$O$_5$ by B$_4$C and graphite at 1600 °C in an alumina tube furnace under following Ar [20]. The measured Young's modulus of TaB$_2$ was 551 GPa, which was higher than ZrB$_2$ and HfB$_2$. In addition, shear modulus of 228 GPa and hardness of 25.6 GPa were observed for TaB$_2$. The most interesting results were that, under the same value of load (4.9 N), the measured hardness (25.6 GPa) [20] of TaB$_2$ is larger than that of ReB$_2$ (18.4 GPa) [21]. This combination of properties makes it potentially useful in applications including cutting tools, high temperature crucibles and thermal protection components.

However, neither the structural nor the electronic properties of TaB$_2$ have been studied theoretically yet. In this work, we performed density functional calculation on the electronic and elastic properties of TaB$_2$ and compared the results with the experiment. TaB, IrB, and IrB$_2$ were also studied in the present work.

2. Computational detail

The calculations presented in this study were performed within the density functional theory, using the projector-augmented wave (PAW) method [22,23] as implemented in Vienna

* Corresponding author. Fax: +86 378 3881602.
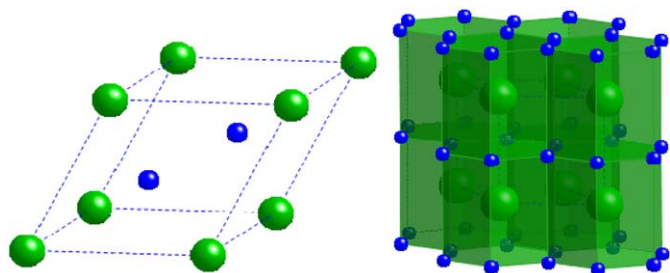*E-mail address:* wangyx@henu.edu.cn (Y.X. Wang).

Fig. 1. Hexagonal structure of TaB_2 with space group $P6/mmm$, The large green and small blue spheres represent the Ta and B atoms, respectively. The shortest B–B bond and Ta–B bond are 1.788 Å and 2.448 Å, respectively. (For interpretation of the references to color in this figure legend, the reader is referred to the web version of this article.)

ab initio simulation package (VASP) [24–26]. Both the generalized gradient approximation (GGA) [27] and the local density approximation (LDA) [28] were used with the PAW potential. The structure was optimized with the conjugate-gradient algorithm method. A plane wave cutoff energy of 500 eV was employed throughout. The calculations were performed using a (18,11,13) Monkhorst–Pack mesh which corresponds to 420 k-points in the irreducible Brillouin zone of the orthorhombic $Pmmn$ structure. The structure optimization of hexagonal TaB_2 and IrB_2 has been performed under the symmetry restriction of space group $P6/mmm$ and $P6_3/mmc$, which are same as those of AlB_2 and ReB_2, respectively. The computational condition for hexagonal TaB_2 and IrB_2 is same as that of the orthorhombic one except the different Monkhorst–Pack mesh (16,16,16) for $P6/mmm$ phase and (22,22,10) for $P6_3/mmc$ phase. For the hexagonal $P6_3/mmc$ TaB and IrB, the calculations were performed using a (16,16,16) Monkhorst–Pack mesh which corresponds to 270 k-points in the irreducible Brillouin zone. In addition, the calculations of temperature dependence of bulk modulus and volume are carried out with quasi-harmonic approximation.

The optimized $P6/mmm$ phase TaB_2 is drawn in Fig. 1. Optimized lattice constants of hexagonal $P6/mmm$ TaB_2 with LDA (GGA) are $a = 3.061$ (3.096) Å and $c = 3.301$ (3.346) Å, which match closely the experimental ones ($a = 3.088$ A, $c = 3.241$ A [16]; $a = 3.082$ A, $c = 3.243$ A [17]). Moreover, our calculated Young's modulus and shear modulus of $P6/mmm$ phase TaB_2 with LDA (GGA) are 587 GPa (531 GPa) and 243 GPa (219 GPa), respectively, which also agree well with experimental data 551 and 228 GPa [20].

3. Results and discussions

We initially considered the structure competing of TaB_2 and IrB_2. This was done by performing first-principle calculations of TaB_2 and IrB_2 with considering a variety of structure types including ReB_2-like, OsB_2-like, AlB_2-like. The calculated lattice constants for TaB_2, TaB, IrB_2, and IrB, are listed in Table 1 together with the corresponding experimental results. It is clear that the predicted lattice parameters with GGA are larger than that with LDA, as the usual case. The calculated lattice parameters for $P6/mmm$ phase TaB_2 with LDA are in excellent agreement with the experimental data [16,17], differing only by 0.87% (0.68%) and 1.85% (1.79%) in comparison with that of Ref. [16,17], respectively. Table 2 lists the calculated equilibrium volume, the relative total energy, the bulk modulus, and its pressure derivative of TaB_2 with the three structures and TaB with $P6_3/mmc$ phase. The bulk modulus and its pressure derivative are obtained by fitting pressures and cell volumes with the third-order Birch–Murnaghan equation of state [29]. From this table, it can be

seen that the $P6/mmm$ structure is more stable in energy than the other ones. Moreover, $P6/mmm$ phase TaB_2 has the smallest cell volume among the three structures, which may result in the higher bulk modulus of the $P6/mmm$ structure. The calculated bulk modulus for TaB with LDA and GGA are 291 and 267 GPa, respectively, which are lower than that of $P6/mmm$ phase TaB_2. From Table 3, $Pmmn$ phase IrB_2 is more stable in energy than the $P6_3/mmc$ and $P6/mmm$ ones. However, the cell volume of $Pmmn$ phase IrB_2 is larger than the $P6_3/mmc$ and $P6/mmm$ ones, and its bulk modulus is slightly higher than that of $P6_3/mmc$ phase but lower than the $P6/mmm$ one. The calculated bulk modulus of IrB with LDA and GGA are 346 and 309 GPa, respectively, which are higher than that of IrB_2.

Table 1
Calculated equilibrium lattice parameters a (Å), b (Å), c (Å) for TaB_2, TaB, IrB_2, and IrB.

			a	b	c
TaB_2	$P6/mmm$	LDA	3.061		3.301
		GGA	3.096		3.346
		Expt. [16]	3.088		3.241
		Expt. [17]	3.082		3.243
	$Pmmn$	LDA	2.958	4.765	4.309
		GGA	3.002	4.824	4.355
	$P6_3/mmc$	LDA	2.951		7.983
		GGA	2.993		8.081
TaB	$P6_3/mmc$	LDA	3.369		4.761
		GGA	3.412		4.821
IrB_2	$Pmmn$	LDA	3.113	4.487	3.993
		GGA	3.153	4.547	4.042
	$P6_3/mmc$	LDA	3.034		6.988
		GGA	3.072		7.074
	$P6/mmm$	LDA	3.080		3.180
		GGA	3.107		3.259
IrB	$P6_3/mmc$	LDA	3.474		3.902
		GGA	3.508		3.986

Table 2
Calculated cell volume (V in A^3), relative total energy (E in eV), bulk modulus (B in GPa), and its pressure derivative at zero pressure (B_1) of TaB_2 and TaB.

			V	E	B	B_1
TaB_2	$P6/mmm$	LDA	26.67	0.00	334	4.12
		GGA	27.77	0.00	308	4.08
	$Pmmn$	LDA	30.37	1.24	273	3.60
		GGA	31.54	1.04	254	3.69
	$P6_3/mmc$	LDA	30.11	1.33	267	3.66
		GGA	31.34	1.16	245	3.79
TaB	$P6_3/mmc$	LDA			292	4.04
		GGA			267	4.07

V and E are of per chemical formula unit.

Table 3
Calculated cell volume (V in A^3), relative total energy (E in eV), bulk modulus (B in GPa), and its pressure derivative at zero pressure (B_1) of IrB_2 and IrB.

			V	E	B	B_1
IrB_2	$Pmmn$	LDA	27.89	0.00	300	3.88
		GGA	28.97	0.00	276	3.89
	$P6_3/mmc$	LDA	27.86	0.13	257	4.88
		GGA	28.91	0.13	246	4.54
	$P6/mmm$	LDA	26.13	1.83	324	4.30
		GGA	27.25	1.78	289	4.34
IrB	$P6_3/mmc$	LDA			346	4.58
		GGA			309	4.52

V and E are of per chemical formula unit.

The mechanical stability is a necessary condition for a crystal to exist. In order to check the elastic stability of TaB_2, TaB, IrB_2, and IrB, their elastic constants were calculated by the strain–stress method. A small finite strain was applied on the optimized structure and then the atomic position was optimized. Then, the elastic constants were obtained from the stress of the strained structure. Table 4 lists the calculated elastic constants for TaB_2 and TaB. The bulk and shear moduli in this table were calculated by the Voigt–Reuss–Hill approximation method [30]. From this table, the bulk modulus agrees with that obtained from the third-order Birch–Murnaghan equation of state. The shear modulus of $P6/mmm$ phase TaB_2 is higher than the $Pmmn$ one. An important reason for the high shear modulus of $P6/mmm$ phase TaB_2 is that the polyhedra in the $Pmmn$ structure are entirely linked by shared edges, whereas the polyhedra in $P6/mmm$ phase share the faces and edges (as shown in Fig. 1) and this structure is expected to be more rigid with respect to shear stress. We calculated the eigenvalues of the elastic constant matrix of the three structures and found that all eigenvalues are positive for $P6/mmm$ and $Pmmn$ phases, which indicates that both $P6/mmm$ and $Pmmn$ structures of TaB_2 are elastically stable. The negative c_{66} (-95 GPa from both LDA and GGA) of $P6_3/mmc$ TaB_2 indicates that it is elastically unstable, and its elastic constants as well as the relevant data are no longer listed in Table 4. Moreover, the calculated Young's modulus 587 GPa (531 GPa) and shear modulus 243 GPa (219 GPa)

of $P6/mmm$ phase TaB_2 with LDA (GGA) are in excellent agreement with the experimental data ($E = 551$ GPa, and $G = 228$ GPa) [20]. As seen in Table 4, $P6/mmm$ TaB_2 has a smaller Poisson's ratio than the $Pmmn$ phase, WB_2 (0.24 Ref. [1]), and OsB_2(0.27 Ref. [3]). Smaller Poisson's ratio implies that $P6/mmm$ phase TaB_2 is relatively stable against shear. For TaB, the calculated bulk and shear moduli are smaller than that of $P6/mmm$ phase TaB_2. From Table 5, the bulk modulus of IrB_2 agrees well with that obtained from the third-order Birch–Murnaghan equation of state. The shear modulus of IrB_2 is only about half of that for $P6/mmm$ phase TaB_2. We also calculated the eigenvalues of the elastic constant matrix of the three structures and found that all eigenvalues are positive for $P6_3/mmc$ and $Pmmn$ phases, which indicates that the $P6_3/mmc$ and $Pmmn$ structures of IrB_2 are both elastically stable. The negative c_{44} (-49 GPa from LDA and -61 GPa GGA) of $P6/mmm$ IrB_2 indicates that it is elastically unstable. The calculated bulk modulus 355 GPa (LDA) of IrB is even larger than that of $P6/mmm$ TaB_2 (334 GPa with LDA), while its shear modulus 168 GPa (LDA) is significantly smaller than that of TaB_2 (243 GPa with LDA). Moreover, larger Poisson's ratio of 0.30 and lower value of G/B (0.46) for IrB exclude its potential superhard property. The phonon band structures of $P6/mmm$ phase TaB_2 under 0 and 50 GPa were computed and the results are shown in Fig. 2. The calculated phonon band structures have no soft mode at any

Table 4
Calculated elastic constants (in GPa), bulk modulus B (in GPa), shear modulus G (in GPa), Young's modulus (E in GPa), Poisson's ratio (v), and G/B of TaB_2 and TaB.

		c_{11}	c_{12}	c_{13}	c_{22}	c_{23}	c_{33}	c_{44}	c_{55}	c_{66}	B	G	E	v	G/B
TaB_2 ($P6/mmm$)	LDA	648	152	232			486	235		248	334	243	587	0.21	0.73
	GGA	598	145	214			442	208		227	308	219	531	0.21	0.71
	Expt. [20]											551			
TaB_2 $Pmmn$	LDA	428	189	116	477	140	704	233	56	206	275	160	402	0.26	0.58
	GGA	418	163	102	456	127	660	219	78	202	255	172	421	0.22	0.67
TaB ($P6_3/mmc$)	LDA	471	197	209			449	282		137	291	208	504	0.21	0.71
	GGA	441	176	188			417	259		133	267	196	472	0.21	0.73

Table 5
Calculated elastic constants (in GPa), bulk modulus B (in GPa), shear modulus G (in GPa), Young's modulus (E in GPa), Poisson's ratio (v), and G/B of IrB_2 and IrB.

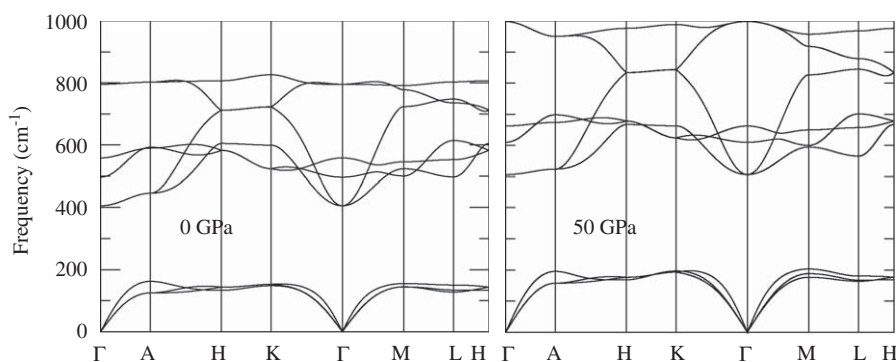|		c_{11}	c_{12}	c_{13}	c_{22}	c_{23}	c_{33}	c_{44}	c_{55}	c_{66}	B	G	E	v	G/B
IrB_2 ($Pmmn$)	LDA	377	273	159	450	188	745	88	73	144	307	118	314	0.33	0.38
	GGA	345	241	139	414	170	669	62	67	137	274	104	277	0.33	0.38
IrB_2 ($P6_3/mmc$)	LDA	331	221	283			775	140			305	113	302	0.34	0.37
	GGA	315	197	254			695	126			280	109	289	0.33	0.39
IrB ($P6_3/mmc$)	LDA	591	261	295			380	189			355	168	435	0.30	0.47
	GGA	525	235	264			338	164			317	146	377	0.30	0.46

Fig. 2. Calculated phonon band structure of hexagonal $P6/mmm$ TaB_2. The special k points A, H, K, M, and L in the figure represent the points $(0, 0, \frac{1}{2})$, $(-\frac{1}{3}, \frac{2}{3}, \frac{1}{2})$, $(-\frac{1}{3}, \frac{2}{3}, 0)$, $(0, \frac{1}{2}, 0)$, and $(0, \frac{1}{2}, \frac{1}{2})$, respectively.

vectors, which confirms the stability of $P6/mmm$ phase TaB_2 under 0 and 50 GPa. With increasing pressure, the vibrational bands of the optical part shift to higher frequencies, while the acoustic part has no obvious change.

As seen in Table 4, TaB_2 with the hexagonal $P6/mmm$ structure have large bulk modulus 334 GPa (LDA) and large shear modulus 243 GPa (LDA). Hardness is a macroscopic concept. Besides the bulk and shear moduli, the elastic constant c_{44} is also an important parameter indirectly governing the indentation hardness. The elastic constant c_{44} of $P6/mmm$ phase TaB_2 is calculated to be 235 GPa (LDA). This value is exceptionally high, as shown in Fig. 3, exceeding the counterparts of WB_2 [1], OsB_2 [3], WB_4 [9], ReC [31], OsN_2 [32], IrN_2 [33], and PtN_2 [34,35]. The elastic constant c_{44} of TaB_2 in hexagonal $P6/mmm$ phase relates to lattice resistance against an applied $[11\bar{2}0]$ (0001) shear deformation. In order to calculate out the theoretical value of hardness and further understand the correlation between the hardness and c_{44}, we first employ the first-principle model of intrinsic hardness [36] to get the hardness of a specific bond. The formula for calculation is as follows:

$$H_v^\mu (GPa) = 740 P^\mu (v_b^\mu)^{-5/3} \qquad (1)$$

where P^μ is Mulliken overlap population of μ-type bond and v_b^μ is the volume of bond of type μ. Then we obtain the material hardness using the following formula:

$$H_v(GPa) = [(H_v^{\mu_1})^{m_1}(H_v^{\mu_2})^{m_2} \cdots (H_v^{\mu_n})^{m_n}]^{1/m_1+m_2+\cdots+m_n} \qquad (2)$$

where m_i is the bond number of type μ_i per unit volume. All the hardness calculations are performed with GGA. The calculated hardness of $P6/mmm$ phase TaB_2 is 37.05 GPa, which is higher than the experimental data 25.6 ± 0.7 GPa [20]. Such a difference between the theoretical value and experiment may be attributed to the large loading force (0.5 kg used in the experiment) [20]. It is noteworthy that, under the same value of load (4.9 N), the measured hardness (25.6 GPa) [20] of TaB_2 is larger than that of ReB_2 (18.4 GPa) [21]. Moreover, our calculated hardness of ReB_2 employing the present method is 41.66 GPa, which is lower than
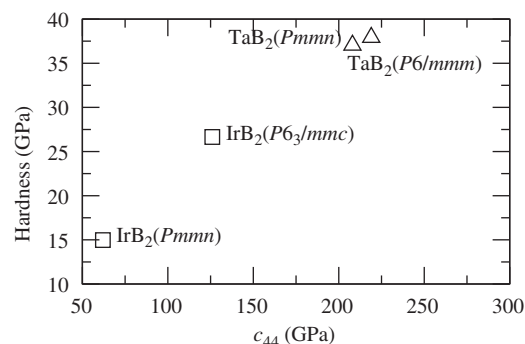
Fig. 4. Hardness as a function of the elastic constants of c_{44} for TaB_2 and IrB_2. The c_{44} correspond to the values within GGA.

the experimental data 48 GPa (measured under a load of 0.49 N) [37] but higher than 37.0 GPa (under 0.72 N) [38]. Based on above analysis, we can predict that the calculated hardness (37.05 GPa) of TaB_2 probably correspond to the experimental data obtained under $0.49-0.72$ N. So, it is not surprising that the calculated hardness is higher than the experimental data measured under 0.5 kg, i.e. 4.9 N. Thus, we hope there will be a uniform measurement standard and method for material hardness measuring. We suggest that the measured micro-hardness of a material be obtained from the steady value at high applied load. For IrB_2, the hardness (14.97 GPa) of the $Pmmn$ structure is smaller than that of $P6_3/mmc$ phase (26.65 GPa). The hardness as a function of the elastic constant c_{44} for $P6/mmm$, $Pmmn$ TaB_2, and $P6_3/mmc$, $Pmmn$ IrB_2 are plotted in Fig. 4. The data of hardness versus c_{44} lie along the same straight line, which prove that c_{44} is a better hardness predictor for transition-metal diborides. The calculated hardness of TaB and IrB are 23.09 and 12.36 GPa, respectively, which are basically proportional to the elastic constants of c_{44}. The relative directionality of the bonding in the material also have an important effect on its hardness and can be determined by the value of G/B [39]. The calculated ratio G/B for TaB_2 in $P6/mmm$ phase (0.72) is much larger than WB_2 (0.63) [1], OsB_2 (0.50) [3], IrN_2 (0.66) [33], and PtN_2 (0.61) [34], indicating the more pronounced directional bonding between the ions in TaB_2 with the $P6/mmm$ structure. The elastic anisotropy (A) of crystals is also important for their applications. The elastic anisotropy of the low-symmetry crystal can be described by the percentage anisotropy in compressibility (A_B) and shear (A_G) [39]. For A_B and A_G, a values of zero and 1 (100%) represent elastic isotropy and the largest anisotropy. For hexagonal $P6/mmm$ TaB_2, the calculated A_B and A_G are 0.31% (0.34%) and 9.02% (8.96%) with LDA (GGA), indicating its little elastic anisotropy. The elastic constants have been used as predictors for high hardness in early DFT calculations. However, since material deformation at large strains usually results in a nonlinear stress–strain relation, it could lead to significant deviations from the simple extrapolation of equilibrium data [40]. Thus, there is reason to be cautiously optimistic about the super hardness estimated only from elastic parameters. The superhard property worked out by the elastic constants is to be further confirmed by calculating the ideal shear strength in the future work.

Shown in Fig. 5 is the calculated band structure with GGA of $P6/mmm$ phase TaB_2. From this figure, it can be seen that some bands cross the Fermi level, which indicates the metallic behavior of $P6/mmm$ phase TaB_2. The calculated total and partial density of states (DOS) proves that TaB_2 with the hexagonal and orthorhombic structures are all metallic. DOS of TaB_2 and IrB_2 with the three structures are plotted in Figs. 6 and 7. As seen in Fig. 6, DOS of $P6/mmm$ TaB_2 is significantly different from that of
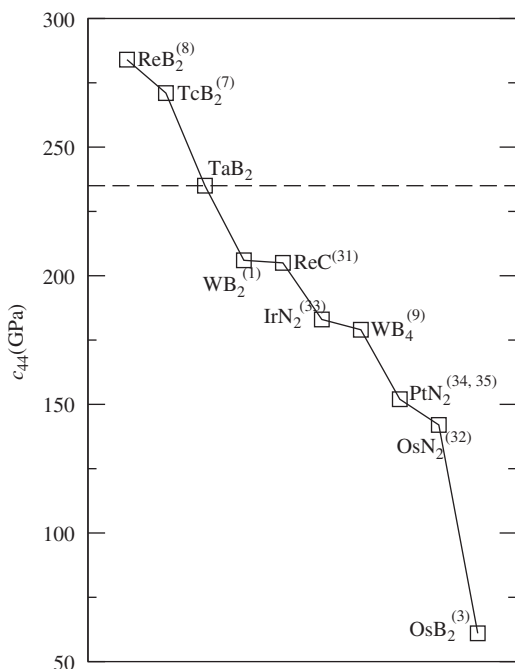

Fig. 3. The elastic constants of c_{44} for different compounds. The superscripts represent the corresponding references from which the data are taken.
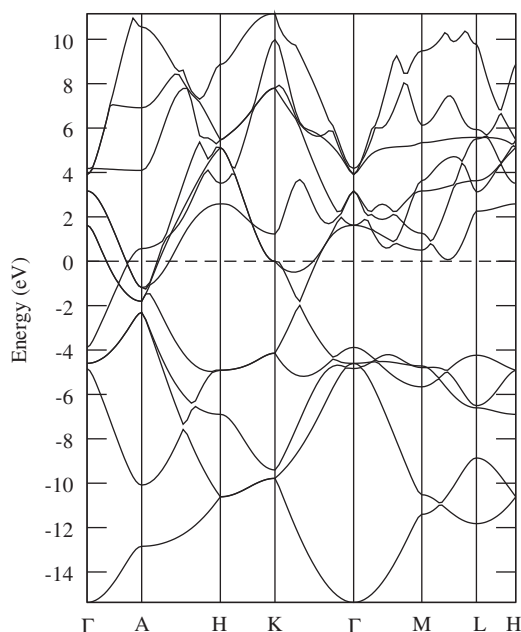
Fig. 5. Band structure of hexagonal $P6/mmm$ TaB$_2$. The high symmetry k points A, H, K, M, and L in the figure represent the points $(0, 0, \frac{1}{2})$, $(-\frac{1}{3}, \frac{2}{3}, \frac{1}{2})$, $(-\frac{1}{3}, \frac{2}{3}, 0)$, $(0, \frac{1}{2}, 0)$, and $(0, \frac{1}{2}, \frac{1}{2})$, respectively.
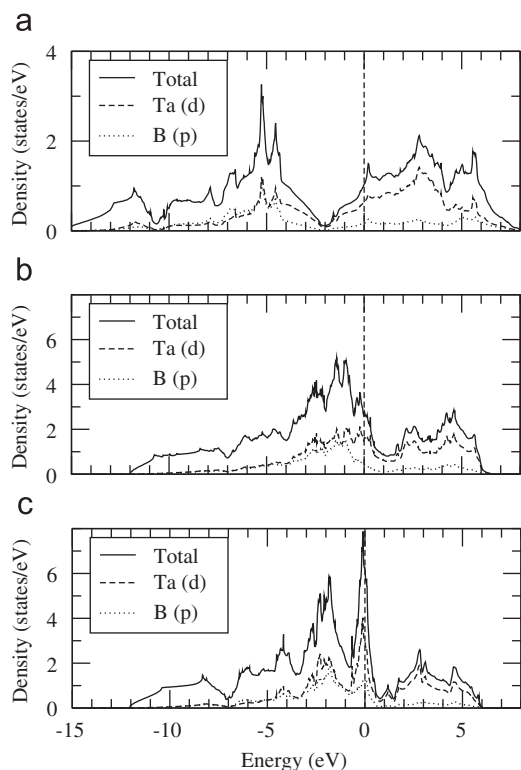

Fig. 7. Total and partial DOS of IrB$_2$: (a) $Pmmn$ phase; (b) $P6_3/mmc$ phase; (c) $P6/mmm$. The Fermi level is at zero.

Fig. 6. Total and partial DOS of TaB$_2$: (a) $P6/mmm$ phase; (b) $Pmmn$ phase; (c) $P6_3/mmc$. The Fermi level is at zero.

the $P6_3/mmc$ and $Pmmn$ ones. Compared with the other two phases, the states around the Fermi level in the $P6/mmm$ phase shift to the lower energy. From Fig. 7, the three phases of IrB$_2$ are also metallic for lack of energy gap near the Fermi level. To gain a more detailed insight into the bonding characters of $P6/mmm$ TaB$_2$, we plot the charge density distribution in (0001) and $(11\overline{2}0)$ planes, as shown in Fig. 8. From this figure, we can see a strong
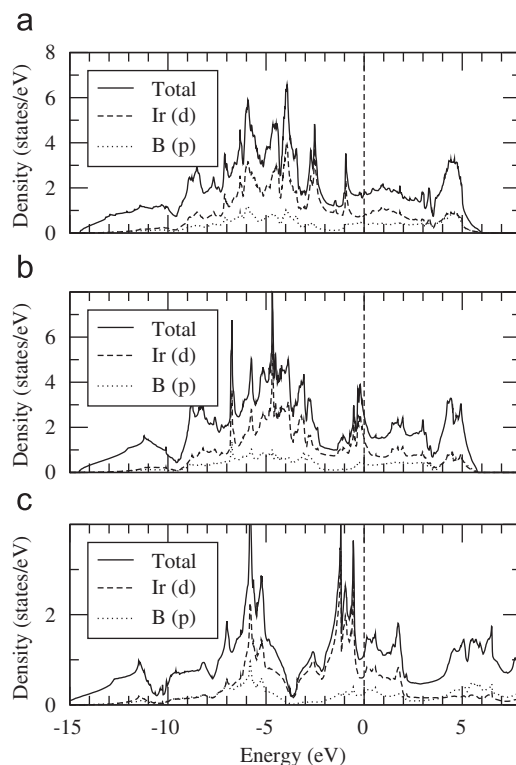
covalent π-bonding of B-hexagon in the (0001) plane, such a B-hexagon network can strongly resist against an applied $[11\overline{2}0]$ (0001) shear deformation. From $(11\overline{2}0)$ plane we can see some electrons between Ta and B atoms, indicating a strong directional covalent Ta–B bonding exists in hexagonal $P6/mmm$ TaB$_2$. Furthermore, two neighbor boron atoms form a very strong covalent bond. It is emphasized that the formation of these directional covalent bonds leads to the increase in the hardness.

Fig. 9(a) shows the normalized volume–temperature diagram of $P6/mmm$ TaB$_2$ within 0–1000 K range. From Fig. 9(a), it can be seen easily that the cell volume increases almost linearly when $T > 300$ K. Fig. 9(b) shows the normalized bulk modulus–temperature diagram of $P6/mmm$ TaB$_2$. As shown in Fig. 9(b), it can be seen that the bulk modulus of TaB$_2$ decreases almost linearly with increasing temperature, which is consistent with the trend of the cell volume. In Fig. 9(c), we present the curve of the heat capacity (C_v) with temperature and pressure in the $P6/mmm$ structure of TaB$_2$. It shows that when $T < 1000$ K, C_v is sensitive to both the temperature and pressure. This is due to the anharmonic approximations of the Debye model. However, when $T > 1000$ K, the anharmonic effect on C_v is suppressed, and C_v is very close to the Dulong–Petit limit.

4. Conclusion

In summary, the three phases of TaB$_2$ are metallic for lack of energy gap near the Fermi level, and $P6/mmm$ phase TaB$_2$ is more stable than the other two phases. All positive eigenvalues of the elastic constant matrix confirms that both $P6/mmm$ and $Pmmn$ phases of TaB$_2$ are elastically stable. The calculated equilibrium structural parameters, shear modulus, and Young's modulus of TaB$_2$ are well consistent with the available experimental data. Our calculated hardness (37.05 GPa) of $P6/mmm$ TaB$_2$ phase is larger
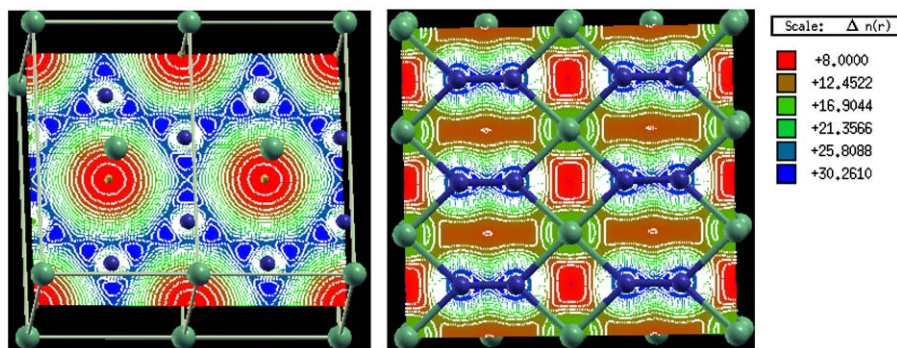
Fig. 8. (Color online) The valence electron density for $P6/mmm$ phase TaB_2 in (0001) (left) and (1120) (right) planes. The bonding between B and B exhibits the strong directionality throughout the plane.
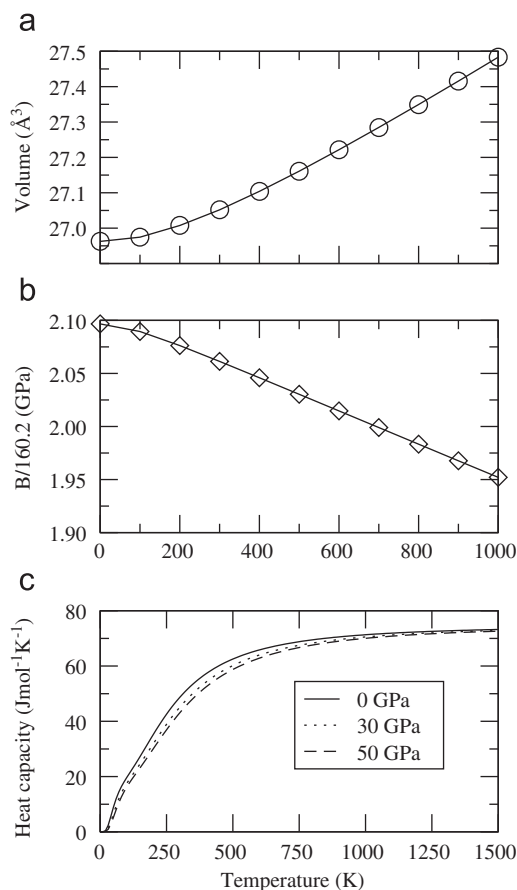

Fig. 9. (a) The variations of the cell volume for $P6/mmm$ TaB_2 versus the temperature. (b) The variations of the bulk modulus for $P6/mmm$ TaB_2 versus the temperature. (c) The heat capacity of $P6/mmm$ TaB_2 at different temperature and pressure.

than the experimental value of 25.6 GPa, which may be attributed to the large loading force (0.5 kg) used in the experiment. So, we hope there will be a uniform measurement standard and method for material hardness measuring. The large G/B value of $P6/mmm$ phase TaB_2 means strong directional bonding in it, which partially corresponds its high hardness. Moreover, the large c_{44} of TaB_2 also contributes to its high hardness. For IrB_2, our calculated results show that the $Pmmn$ structure is the most stable phase in energy, and its hardness (14.97 GPa) is smaller than that of the $P6_3/mmc$ structure (26.65 GPa). For TaB and IrB, all positive eigenvalues of the elastic constant matrix confirm that they are both elastically stable in $P6_3/mmc$ phase. The calculated hardness for TaB and IrB are 23.09 and 12.36 GPa, respectively, which are much smaller than that of $P6/mmm$ phase TaB_2.

Acknowledgments

References

[1] X.F. Hao, Y.H. Xu, Z.J. Wu, D.F. Zhou, X.J. Liu, X.Q. Cao, J. Meng, Phys. Rev. B 74 (2006) 224112.
[2] R.W. Cumberland, M.B. Weinberger, J.J. Gilman, S.M. Clark, S.H. Tolbert, R.B. Kaner, J. Am. Chem. Soc. 127 (2005) 7264.
[3] H.Y. Gou, L. Hou, J.W. Zhang, H. Li, G.F. Sun, F.M. Gao, Appl. Phys. Lett. 88 (2006) 221904.
[4] S. Chiodo, H.J. Gotsis, N. Russo, E. Sicilia, Chem. Phys. Lett. 425 (2006) 311.
[5] M. Hebbache, L. Stuparević, D. Živković, Solid State Commun. 139 (2006) 227.
[6] Z.Y. Chen, H.J. Xiang, J.L. Yang, J.G. Hou, Q.S. Zhu, Phys. Rev. B 74 (2006) 012102.
[7] Y.X. Wang, Appl. Phys. Lett. 91 (2007) 101904.
[8] Y.C. Liang, B. Zhang, Phys. Rev. B 76 (2007) 132101.
[9] M. Wang, Y.W. Li, T. Cui, Y.M. Ma, G.T. Zou, Appl. Phys. Lett. 93 (2008) 101905.
[10] X.L. Zhu, D.H. Li, X.L. Cheng, Solid State Commun. 147 (2008) 301.
[11] Q.F. Gu, G. Krauss, W. Steurer, Adv. Mater. 20 (2008) 3620.
[12] S.J. La Placa, B. Post, Acta Crystallogr. 15 (1962) 97.
[13] T. Lundström, Ark. Kemi 30 (1969) 115.
[14] H.P. Woods, F.E. Wawner Jr., B.G. Fox, Science 151 (1966) 75.
[15] P. Schwarzkopf, R. Kieffer, W. Leszynski, F. Benesovsky, Refractory Hard Metals: Borides, Carbides, Nitrides, and Silicides, The Macmillan Company, New York, 1953.
[16] J.T. Norton, H. Blumenthal, S.J. Sindeband, Trans. AIME 185 (1949) 749.
[17] D. Kaczorowski, A.J. Zaleski, O.J. Żogal, J. Klamut, cond-mat/0103571, 2001.
[18] V.I. Matkovich, G.V. Samsonov, P. Hagenmuller, T. Lundstrom, Boron and Refractory Borides, Spring, Berlin, Heidelberg, New York, 1977.
[19] R.A. Cutler, in: S.J. Schneider (Ed.), Ceramics and Glasses: Engineered Materials Handbook, vol. 4, ASM International, USA, 1991, p. 787.
[20] X.H. Zhang, G.E. Hilmas, W.G. Fahrenholtz, Math. Lett. 62 (2008) 4251.
[21] J.Q. Qin, D.W. He, J.H. Wang, L.M. Fang, L. Lei, Y.J. Li, J. Hu, Z.L. Kou, Y. Bi, Adv. Mater. 20 (2008) 1.
[22] G. Kresse, D. Joubert, Phys. Rev. B 59 (1999) 1758.
[23] P.E. Blöchl, Phys. Rev. B 50 (1994) 17953.
[24] G. Kresse, J. Hafner, Phys. Rev. B 47 (1993) 558.
[25] G. Dresse, J. Hafner, J. Phys. Condens. Matter 6 (1994) 8245.
[26] G. Kresse, J. Furthmüller, Phys. Rev. B 54 (1996) 11169.
[27] J.P. Perdew, K. Burke, M. Ernzerhof, Phys. Rev. Lett. 77 (1996) 3865.
[28] D.M. Ceperley, B.J. Alder, Phys. Rev. Lett. 45 (1980) 566.
[29] F. Birch, Phys. Rev. 71 (1947) 809.
[30] R. Hill, Proc. Phys. Soc. London 65 (1952) 349.

[31] Y.X. Wang, Phys. Status Solidi 2 (2008) 126.
[32] Y.X. Wang, M. Arai, T. Sasaki, Appl. Phys. Lett. 90 (2007) 061922.
[33] Y.X. Wang, M. Arai, T. Sasaki, C.Z. Fan, Phys. Rev. B 75 (2007) 104110.
[34] R. Yu, Q. Zhan, X.F. Zhang, Appl. Phys. Lett. 88 (2006) 051913.
[35] H.Y. Gou, L. Hou, J.W. Zhang, G.F. Sun, L.H. Gao, F.M. Gao, Appl. Phys. Lett. 89 (2006) 141910.
[36] F.M. Gao, Phys. Rev. B 73 (2006) 132104.
[37] H.Y. Chung, M.B. Weinberger, J.B. Levine, A. Kavner, J.M. Yang, S.H. Tolbert, R.B. Kaner, Science 316 (2007) 436.
[38] H.Y. Chung, M.B. Weinberger, J.M. Yang, S.H. Tolbert, R.B. Kaner, Appl. Phys. Lett. 92 (2008) 261904.
[39] P. Ravindran, L. Fast, P.A. Korzhavyi, B. Johansson, J. Wills, O. Eriksson, J. Appl. Phys. 84 (1998) 4891.
[40] Y. Zhang, H. Sun, C.F. Chen, Phys. Rev. B 73 (2006) 064109.